Experimental and Theoretical Study of the n-Doped Successive Polyanions of Oligocruciform Molecular Wires: Up to Five Units of Charge

Abdelaziz Al Ouahabi, Paul Baxter, Claude Mathis, Maxime Bernard, Bertrand Vileno, Jean-Paul Gisselbrecht, Philippe Turek, Jean-Marie Mouesca, Sylvie Choua

Experimental and Theoretical Study of the n-Doped Successive Polyanions of Oligocruciform Molecular Wires: Up to Five Units of Charge

Abdelaziz Al Ouahabi,[c] Paul Baxter,[c] Claude Mathis,[c] Maxime Bernard,[a] Bertrand Vileno,[a] Jean-Paul Gisselbrecht,[a] Philippe Turek,[a] Jean-Marie Mouesca,*[b] and Sylvie Choua*[a]

The electronic structure of polyanions of sterically encumbered triisopropylsilyl-substituted linear and cyclic oligo(phenyleneethynylene)s (**M**onomer, **T**rimer, **P**entamer, and **Tri**angle) is investigated by electron paramagnetic resonance (EPR), electron nuclear double resonance (ENDOR), and UV/Vis–near-infrared (NIR) spectroscopies, cyclic voltammetry, and theoretical calculations (DFT). Increasing anion orders are generated sequentially in vacuo at room temperature by chemical reaction with potassium metal up to the pentaanion. The relevance of these compounds acting as electron reservoirs is thus demonstrated. Even-order anions are EPR silent, whereas the odd species exhibit different signatures, which are identified after comparison of the measured hyperfine couplings by ENDOR spectroscopy with those predicted by DFT calculations. With increasing size of the oligomers the electron spin density is first distributed over the backbone carbon atoms for the monoanions, and then further localized at the outer phenyl rings for the trianion species. Examination of the UV/Vis-NIR spectra indicates that the monoanions ($\mathbf{T}^{\bullet-}$, $\mathbf{P}^{\bullet-}$) exhibit two transitions in the Vis-NIR region, whereas a strong absorption in the IR region is solely observed for higher reduced states. Electronic transitions of the neutral monoanions and trianions are redshifted with increasing oligomer size, whereas for a given oligomer a blueshift is observed upon increasing the charge, which suggests a localization of the spin density.

1. Introduction

Since the discovery of semiconducting polymers,[1] molecular electronics has been stimulated by both academia and industry. In this context, numerous experimental and theoretical efforts have been focused on π-conjugated organic polymers. These are finding practical applications in organic electronic devices, although they are better considered as prototypes for their commercial use, such as in light-emitting diodes, solar cells, and field-effect transistors. The rapidly growing area of flexible electronics is thus being currently explored.[2] Accordingly, conjugated oligomers and polymers based on π-molecular monomer units, such as pyrrole, phenylene, thiophene, *p*-phenylenevinylene, and phenyleneethynylene (PE), have been studied extensively because of their optical, electronic, and mechanical properties of interest for molecular electronics.[3–5] Notably, most studies have been devoted to the neutral state or p-doping of conjugated derivatives whereas n-doped materials have been less investigated. The desired development of reliable and efficient devices has shown the need for a basic understanding of charge transport and its relationship to molecular conformation. Nevertheless, a complete understanding of the electrical properties so as to permit the elaboration of operating devices has not yet been achieved. Therefore, the study of the changes of the electronic structure of model compounds upon doping is still of interest. Note that finite-length oligomers are clearly simpler models to be considered for basic investigations rather than polymers. The emergence of nanoscience and nanotechnology has brought forth an interest in poly(phenyleneethynylene) (PPE) and oligo(phenyleneethynylene) (OPE) derivatives, since these are actually appropriate model systems of molecular conducting wires, both experimentally and theoretically.[6–17] This interest is motivated by the expected rigid-rod behavior of the conjugated backbone, which preserves π conjugation promoting charge delocalization. However, the low barrier to rotation about the phenyl–ethynyl bridge may induce twisted conformations especially in fluid solution, which may affect the wire conductance and electronic transitions. OPEs have also been studied extensively with respect to their photophysical properties.[18–31] However, due to the ease of aggregation by π–π stacking[32,33] and the resulting complex synthetic strategies to overcome it, little work has been devoted to the experimental study of doped OPEs and especially of highly charged species with more than one added electron. Creating electrical charges upon doping is

[a] *M. Bernard, Dr. B. Vileno, Dr. J.-P. Gisselbrecht, Prof. P. Turek, Dr. S. Choua*
Institut de Chimie (UMR 7177)
Université de Strasbourg
4 rue Blaise Pascal, CS 90032, 67081 Strasbourg Cedex (France)
E-mail: sylvie.choua@unistra.fr

[b] *Dr. J.-M. Mouesca*
CEA Grenoble, INAC/SCIB, UMR-E3 (CEA UJF)
17 rue des Martyrs, 38054 Grenoble Cedex 9 (France)
E-mail: jean-marie.mouesca@cea.fr

[c] *Dr. A. Al Ouahabi, Dr. P. Baxter, Dr. C. Mathis*
Institut Charles Sadron, CNRS, UPR 22
23 rue du Loess, 67034 Strasbourg (France)

the main way to improve the poor conducting properties of the pristine π-conjugated materials. Basic concepts peculiar to molecular conductors have been elaborated to understand the nature of charge carriers in more or less extended π-conjugated materials, such as polarons and bipolarons.[34–37]

Chemical n-doping or p-doping to obtain highly charged species may be performed through various pathways. In the case of n-doping a powerful reducing agent is required and an anionic complex consisting of negatively charged oligomer and counter cations is formed. Of interest are the combined spectroscopic, e.g. UV/Vis–near-infrared (NIR) and electron paramagnetic resonance (EPR), and theoretical (DFT) investigations of n- and/or p-doped species.[38–45] Although scarce, such studies are expected to offer a detailed survey of the electronic processes involved through doping.[46]

As previously mentioned, to discard aggregation and to improve solubility requires synthetic efforts to produce model OPE compounds with bulky side and/or terminal alkyl or silyl groups. The synthesis of a series of OPEs with side triisopropylsilyl (TIPS) and end trimethylsilyl (TMS) substituents was recently reported.[47] TIPS substituents are expected to increase the solubility of the oligomers and they are bulky protecting groups that may stabilize charged oligomers.

Herein, we report the combined EPR/electron nuclear double resonance (ENDOR) spectroscopy, UV/Vis-NIR spectroscopy, and cyclic voltammetry studies of charged species obtained by multiple reduction of some of these sterically encumbered TIPS-oligo[*n*]cruciforms (Scheme 1). TIPS-dehydrotribenzo[12]annulene (**Tr**, Scheme 1) was also investigated to compare encumbrance on the cyclic analogue.

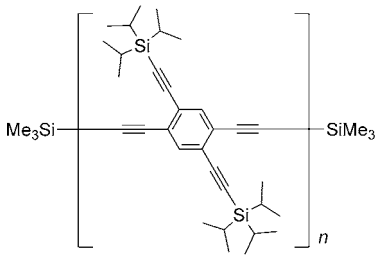

n = 1 **M**
n = 3 **T**
n = 5 **P**

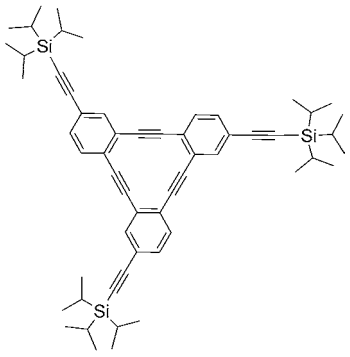

Tr

Scheme 1. Molecular scheme of the studied oligocruciforms **M**, **T**, **P**, and **Tr**.

Molecular orbital (MO) calculations were performed with DFT to investigate the electronic structure of these *n*-anions with $n = 1$–5 on moving from the monomer to the pentamer, that is, as many electrons (and even $n+1$ in some cases) could be accommodated as the number of TIPS-PE monomer units. Notably, similar but less encumbered oligomers were previously investigated with the aim of probing the efficiency of the through-bond magnetic exchange interaction between spin carriers located at the 1,4-termini.[48–50] Given 1) the required computational time and the computational difficulties to manage such encumbered molecules of increasing size, and 2) the quite rare collection of the complementary ENDOR and EPR data of highly negatively charged species, the computation of the EPR parameters has been focused on, that is, hyperfine coupling constants (HFCCs). UV/Vis-NIR spectroscopic investigations were conducted mostly to monitor the achievement of the successive polyanions.

2. Results

Electrochemistry

Electrochemical investigations of the monomer **M**, trimer **T**, pentamer **P**, and [12]annulene species **Tr** were carried out by cyclic voltammetry in THF + 0.1 M Bu_4NPF_6 under vacuum. Some of the results for **M** (compound **10** in ref. [47]), **T** (compound **1** in ref. [47]), and **Tr** (compound **5** in ref. [47]) were previously reported in CH_2Cl_2 dilute solutions. As the present study of multiple anions was performed in THF dilute solutions, the former studies have been completed upon adding the properties of the pentamer **P** species. Therefore, all data are reported in THF dilute solution. The species undergo several electron transfers, which are shown in Figure S1 in the Supporting Information and summarized in Table 1. At a scan rate of 0.1 V s^{-1}, the monomer **M** undergoes one reversible electron

Table 1. Electrochemical data observed by cyclic voltammetry (CV; scan rate $v = 0.1$ V s^{-1}) in THF + 0.1 M Bu_4NPF_6. All potentials are given versus ferrocene, used as internal standard and uncorrected from ohmic drop.

Species	CV [0.1 V s^{-1}]		
	E°[a] [$V_{Fc^+/Fc}$]	ΔE_p[b] [mV]	E_p[c] [$V_{Fc^+/Fc}$]
M	−2.27	180	
			−2.87
			−3.12
T	−1.93	85	
	−2.12	80	
			−2.76[d]
P	−1.81	60	
	−1.90	60	
	−2.13	60	
			−2.40[e]
Tr	−1.84	80	
	−2.13		

[a] $E^{\circ} = (E_{pc} + E_{pa})/2$, where E_{pc} and E_{pa} correspond to the cathodic and anodic peak potentials, respectively. [b] $\Delta E_p = E_{pa} - E_{pc}$. [c] E_p = irreversible peak potential. [d] Reversible behavior at scan rate > 20 V s^{-1} ($E^{\circ} = -2.63$ V vs Fc^+/Fc). [e] At scan rate > 50 V s^{-1} two reversible electron transfers at −2.30 and −2.77 V versus Fc^+/Fc could be observed.

transfer, at −2.27 V versus Fc^+/Fc, followed by two irreversible electron transfers. For the latter, no reversible behavior could be observed for reduction steps two and three by increasing the scan rate. The trimer **T** undergoes two reversible one-electron transfers at −1.93 and −2.12 V versus Fc^+/Fc as well as a third irreversible electron transfer. It has to be mentioned here that the latter became reversible at scan rates higher than 20 $V s^{-1}$. The pentamer **P** gives three reversible one-electron transfers at −1.81, −1.90, and −2.13 V versus Fc^+/Fc followed by irreversible electron transfers. For scan rates higher than 10 $V s^{-1}$, the fourth electron transfer became reversible ($E^\circ = -2.63$ V), whereas at scan rates higher than 50 $V s^{-1}$, a fifth reversible one-electron transfer could be observed at $E^\circ = -2.77$ V. The investigations show clearly that, under our experimental conditions, the reductions occurring at a potential more negative than −2.3 V were irreversible due to a fast follow-up chemical reaction (electrochemical–chemical electron-transfer mechanism).

It has not been excluded that the generated species at negative potentials, which are strong bases, react for example with residual water or even undergo proton abstraction from the tetraalkylammonium salt (Hofmann elimination) and therefore undergo protonation.[51] By increasing the scan rate it was possible, for the trimer **T** and the pentamer **P**, to reach reversibility for these electron transfers. The reduction of **Tr** occurred in two reversible one-electron steps (see Figure S1) at −1.84 and −2.13 V, respectively. At the timescale of cyclic voltammetry the electrogenerated species are stable. Due to the high reactivity of the electrogenerated species at potentials more negative than −2.3 V, electrolysis cannot be used to generate reduced species for EPR measurements. Therefore chemical reductions were carried out in more drastically dried media in the absence of proton donors.

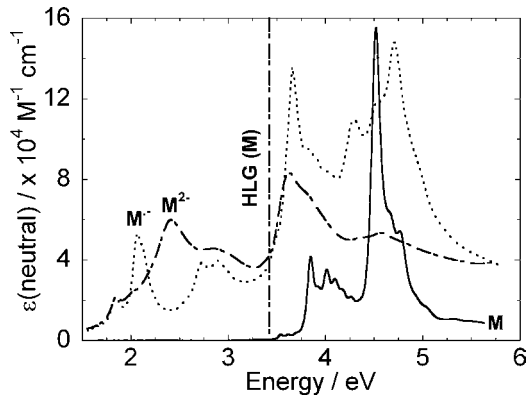

Figure 1. UV/Vis-NIR optical spectrum of neutral **M** and its successive anions, radical monoanion $\mathbf{M}^{\bullet-}$ and dianion $\mathbf{M}^{2-}$, recorded in THF solution. The vertical dashed-dotted line shows the optical bandgap of the neutral species.[47] HLG = HOMO–LUMO energy gap.

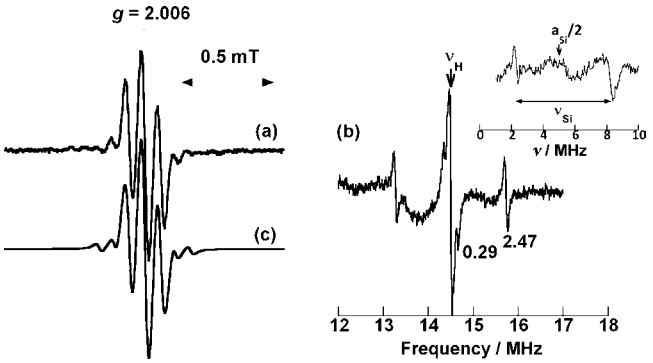

Figure 2. a) EPR spectrum of $\mathbf{M}^{\bullet-}$ in THF solvent at room temperature. b) ^1H ENDOR and ^{29}Si ENDOR spectra of $\mathbf{M}^{\bullet-}$ at room temperature. The numbers under the signals are the $a(^1H)$ values in MHz. c) Simulation with the coupling constants a_H extracted from ^1H ENDOR spectrum.

EPR/ENDOR and UV/Vis-NIR Spectroscopic Studies

Monomer, M

Upon successive short contacts with a potassium mirror, a gradual change to green was observed and monitored step by step with UV–visible spectroscopy. Figure S2 shows the chronological spectral evolution with the appearance and growth of new absorption bands with a main peak at 2.07 eV (600 nm) and additional bands at 2.73 eV (454 nm) and 2.89 eV (429 nm), which correspond to the monoanion. Such monitoring allowed selection of the different anions in large excess relative to the previous and next state. Figure 1 shows the UV/Vis-NIR optical spectrum of the $Q = 0, -1, -2$ charged states of this monomer. New low-energy bands are clearly observed upon electron addition.

The first reduced state is a radical anion, for which the EPR spectrum shows three main lines (1:2:1) centered at $g = 2.006$ (Figure 2a). These are ascribed to the coupling of the unpaired electron with two equivalent ^1H nuclei. Additional lines in the wings are attributed to the coupling of ^{29}Si nuclei (nuclear spin $I = {}^1/_2$, natural abundance 4.67%). The corresponding ^1H HFCCs are also clearly resolved in the ENDOR spectrum in Figure 2b (2.47 MHz) with one additional ^1H HFCC (0.29 MHz). Note that such weak splitting is beyond the magnetic field resolution of EPR spectroscopy (Table 2). Narrowing the ENDOR frequency range allowed the detection of smaller ^1H HFCCs (0.06 MHz, Figure S3). ^{29}Si ENDOR resonance is also observed at half of the hyperfine coupling of ^{29}Si (inset of Figure 2b).

Upon further reduction from $\mathbf{M}^{\bullet-}$ to $\mathbf{M}^{2-}$ the absorption band at 2.07 eV (600 nm) drastically decreases and a new absorption band appears at 2.41 eV (514 nm) accompanied by a color change of the solution from green to red (Figure S2). The dianion is EPR silent, probably due to strong spin pairing of the added electrons. Notably, a weak and broad signal is solely observed, which is testimony of an unresolved signal of $\mathbf{M}^{\bullet-}$ as revealed by the slight color change of the upper top of the solution 1 h after the beginning of the reduction process.

Trimer, T

The study of trimer **T** with the generation of its successive anions was performed as for **M** (Figure S2). The absorption spectrum of neutral **T** shows an intense band at 4.48 eV

Table 2. Experimental HFCCs [MHz] in THF determined from ENDOR spectra and DFT HFCCs calculated at the B3LYP/6-31+G(d) level for monoanions, trianions, and pentaanions.

	$^1H_{1,2}$		$^1H_{3,4}$		$^1H_{5,6}$		$^1H_{7,8}$		$^1H_{9,10}$		^{29}Si	*g* value
	Exp.	Calc.	Exp.	Calc.	Exp.	Calc.	Exp.	Calc.	Exp.	Calc.	Exp.	Exp.
$\mathbf{T}^{\bullet-}$	1.42	0.42	2.15	−1.0	3.02	1.25						2.006
	0.43	0.27										
$\mathbf{P}^{\bullet-}$	–	0.03	0.92(×2)	−0.31	0.52(×2)	0.13	1.25(×2)	−0.73	1.25(×2)	0.71		2.006
	–	0.06			0.92(×2)	0.40						
	Exp.	Calc.	Exp.	Calc.	Exp.	Calc.						
$\mathbf{M}^{\bullet-}$	2.47(×2)	3.55	–	–	–	–	–	–	–	–	10.5(×1)	2.006
$\mathbf{T}^{\bullet3-}$	2.04(×2)	3.52	1.3(×2)	3.14	1.0(×2)	1.55	–	–	–	–	8.4(×1)	2.006
$\mathbf{P}^{\bullet3-}$	0.60(×2)	1.4	1.27(×2)	2.34	1.6(×2)	−2.98	1.6(×2)	3.26	1.27(×2)	2.43		2.006
$\mathbf{P}^{\bullet5-}$	3.08(×2)	3.1									17.0(×1)	
	$H_{1,2,3}$		$H_{4,5,6}$		$H_{7,8,9}$							
$\mathbf{Tr}^{\bullet-}$	4.54(×3)	−5.46	0.17(×3)	0.26	0.34	–	–	–	–			2.006
				0.34	0.22							
				0.47	0.21							

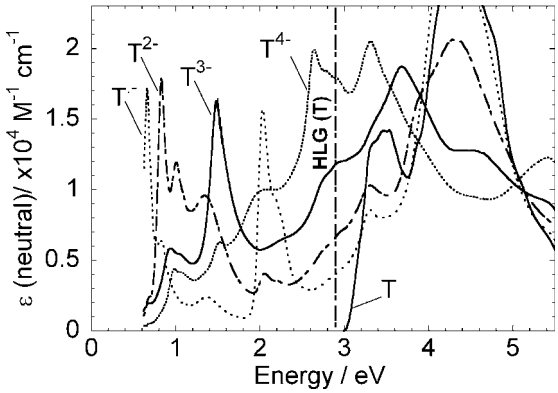

Figure 3. UV/Vis–NIR optical spectra of neutral **T** and its successive anions, monoanion $\mathbf{T}^{\bullet-}$, dianion $\mathbf{T}^{2-}$, and trianion $\mathbf{T}^{\bullet3-}$, recorded in THF solution. The intense absorption peak at 4.48 eV (277 nm) is saturated for **T** and $\mathbf{T}^{\bullet-}$ to obtain the details of the low-energy transitions. The vertical dashed-dotted line shows the optical bandgap of the neutral species.[47]

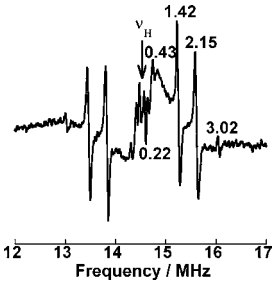

Figure 4. ^{1}H ENDOR spectrum of $\mathbf{T}^{\bullet-}$ at 190 K. The numbers above and under the signals are the $a(^1H)$ values in MHz.

(277 nm; Figure 3). As the reduction proceeds, two new absorption bands appear at low energy at 0.66 eV (1885 nm) and 2.03 eV (611 nm), thus indicating the formation of the radical anion $\mathbf{T}^{\bullet-}$. Upon further contact with the potassium mirror the transformation of $\mathbf{T}^{\bullet-}$ to the dark blue dianion $\mathbf{T}^{2-}$ is indicated by a peak at 0.83 eV (1495 nm). The trianion $\mathbf{T}^{\bullet3-}$ is characterized by a main peak at approximately 1.5 eV (840 nm). Note that a fourth reduction step was achieved but the resulting $\mathbf{T}^{4-}$ species was not as stable as its precursory states.

A seven-line EPR spectrum is observed at room temperature for the radical anion $\mathbf{T}^{\bullet-}$ (Figure S4a). The ^{1}H ENDOR spectrum depends markedly on temperature, due probably to conformational mobility of the phenyl ring connected to the triple bond. ENDOR spectroscopy was performed at lower temperature (≈190–200 K) to enhance the resolution of small HFCCs to obtain $a(^1H) = 3.02$, 2.15, 1.42, 0.43, 0.22 MHz (Figure 4), whereas only three HFCCs could be extracted at room temperature: $a(^1H) = 3.0$, 1.96, 1.46 MHz (Figure S4b).

Simulation of the central part of the EPR spectrum of $\mathbf{T}^{\bullet-}$ is not fully achieved if considering different sets of two protons or one proton. The interpretation of the EPR spectrum is complicated by the probable coexistence of two rapidly averaging conformations. This is suggested by DFT calculations as later discussed. Additional lines in the wings of the EPR spectrum were attributed to ^{29}Si nuclei. Further reduction of $\mathbf{T}^{\bullet-}$ leads to the EPR-silent dianion $\mathbf{T}^{2-}$ in a similar way to that reported for $\mathbf{M}^{2-}$. The peak of maximum absorption in the low-energy region of the optical absorption spectrum of $\mathbf{T}^{2-}$ (Figure 3) is blueshifted with respect to $\mathbf{T}^{\bullet-}$ (0.83 eV/1495 nm vs 0.66 eV/1885 nm).

The stable trianion radical $\mathbf{T}^{\bullet3-}$ was isolated upon further reduction, and showed a blueshift of the low-energy absorption peak (Figure 3) with respect to the mono- and dianion (1.48 eV/840 nm). The EPR spectrum of this species exhibits a well-defined hyperfine pattern centered at $g = 2.006$ (Figure 5a). It is characterized by seven principal lines and a narrower spectral width than $\mathbf{T}^{\bullet-}$. Four ^{1}H HFCCs are given by the ENDOR spectrum (2.04, 1.30, 1.0, 0.15 MHz; Figure 5b) leading to a consistent simulation of the EPR spectrum (Figure 5c). External lines on the EPR spectrum were attributed to ^{29}Si nuclei.

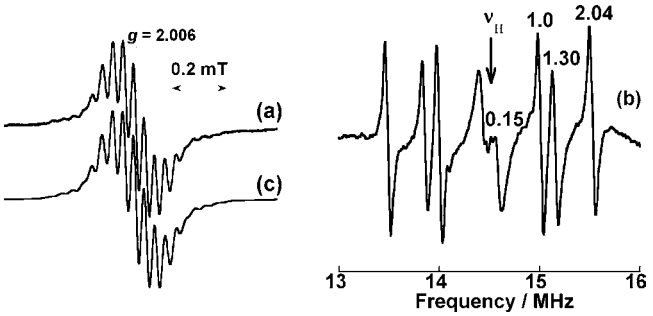

Figure 5. a) EPR spectrum of $\mathbf{T}^{\bullet 3-}$ in THF solvent recorded at room temperature. b) ^{1}H ENDOR spectrum of $\mathbf{T}^{\bullet 3-}$ recorded at room temperature. The numbers above the signals are the values of $a(^1\text{H})$ in MHz. c) Simulation with the use of the coupling constants $a(^1\text{H})$ extracted from the ^{1}H ENDOR spectrum.

This has been implemented in the simulation of the EPR spectrum (Table 2).

Pentamer, P

Similarly, the successive anions of pentamer **P** were investigated by EPR and UV/Vis optical absorption spectroscopy (Figure S2) up to the pentaanion $\mathbf{P}^{\bullet 5-}$. The corresponding UV/Vis-NIR spectra are displayed in Figure 6. The overall features of the UV/Vis-NIR absorption spectra are similar to those observed for the trimer up to the trianion $\mathbf{P}^{\bullet 3-}$, that is, narrow low-energy transitions are observed for the successive anions. The main absorption peaks are blueshifted from 0.54 eV (2240 nm) for $\mathbf{P}^{\bullet -}$ to 0.63 eV (1975 nm) for $\mathbf{P}^{2-}$ and to 0.76 eV (1630 nm) for $\mathbf{P}^{\bullet 3-}$. Notice that $\mathbf{P}^{\bullet -}$ shows two low-energy transitions, as does $\mathbf{T}^{\bullet -}$. Successive transformations could not be monitored from $\mathbf{P}^{\bullet 3-}$ to $\mathbf{P}^{\bullet 5-}$ as precisely as from $\mathbf{P}^{\bullet -}$ to $\mathbf{P}^{\bullet 3-}$, since isosbestic points are not well defined (Figure S2). This suggests the probable simultaneous presence of the next and/or previous anion in the corresponding solutions.

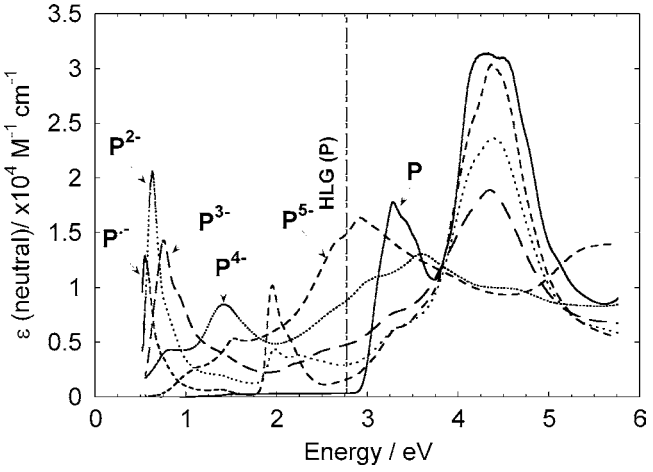

Figure 6. UV/Vis–NIR optical spectra of neutral **P** and its successive anions, monoanion $\mathbf{P}^{\bullet -}$, dianion $\mathbf{P}^{2-}$, trianion $\mathbf{P}^{\bullet 3-}$, tetraanion $\mathbf{P}^{4-}$, and pentaanion $\mathbf{P}^{\bullet 5-}$, recorded in THF solution. The vertical dashed-dotted line shows the optical bandgap of the neutral species.[47]

In spite of two close reduction waves in cyclic voltammetry (Table 1), $\mathbf{P}^{\bullet -}$ could be isolated by chemical reduction as indicated by the optical absorption spectra and by EPR spectroscopy. The spectrum consists of a broad line with poorly defined shoulders (Figure 7 a) extending over a narrower field range than that observed for $\mathbf{T}^{\bullet -}$. The lack of structure in the EPR line is explained by the increasing number of interacting nuclei and the extended delocalization of the unpaired electron, thus building an envelope for a large number of small HFCCs. A ^{1}H ENDOR spectrum is recorded at room temperature (Figure 7 b) with three pairs of ^{1}H lines (1.25, 0.92, 0.52 MHz) and one collapsing line at the pump position ν_H, which are used for simulating the EPR spectrum (Figure 7 c).

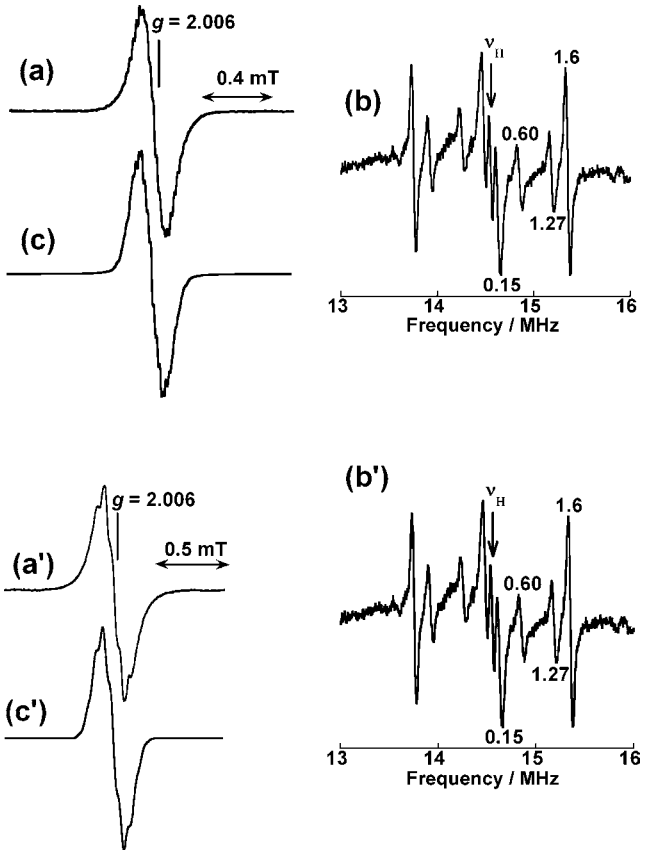

Figure 7. EPR spectrum in THF solvent at 300 K of a) $\mathbf{P}^{\bullet -}$ and a′) $\mathbf{P}^{\bullet 3-}$. Simulation of the EPR spectrum of c) $\mathbf{P}^{\bullet -}$ and c′) $\mathbf{P}^{\bullet 3-}$ with the use of the $a(^1\text{H})$ coupling constants extracted from the ^{1}H ENDOR spectrum at 200 K of b) $\mathbf{P}^{\bullet -}$ and b′) $\mathbf{P}^{\bullet 3-}$. The numbers above and under the signals are the $a(^1\text{H})$ values in MHz.

Further reduction leads to the stable dianion $\mathbf{P}^{2-}$, which is EPR silent as observed for the $\mathbf{M}^{2-}$ and $\mathbf{T}^{2-}$ dianions. As the contact with the K mirror further proceeds, trianion $\mathbf{P}^{\bullet 3-}$ is obtained with an EPR spectrum (Figure 7 a′) similar to that of the monoanion although more structured. The ^{1}H ENDOR spectrum (Figure 7 b′) is different from that of the monoanion with four ^{1}H HFCCs, which allowed simulation of the EPR spectrum (Figure 7 c′ and Table 2). The stable tetraanion $\mathbf{P}^{4-}$ is the next stable state, which is EPR silent. The pentaanion $\mathbf{P}^{\bullet 5-}$ could be isolated and it shows an EPR spectrum with a central triplet due to the coupling of two equivalent protons (Figure S5). As

for other radical anions, additional satellite lines are attributed to ^{29}Si nuclei.

TIPS-Dehydrotribenzo[12]annulene, Tr

On placing into contact with a potassium mirror, a THF solution of the cyclic compound **Tr** turns into an intense green color indicating the monoanion **Tr**$^{\bullet-}$. The optical absorption spectrum of **Tr**$^{\bullet-}$ is drastically modified relative to the neutral species (Figure S6). The complex vibronic structure featuring the peaks of the neutral species shows a different structure for **Tr**$^{\bullet-}$ with enhanced absorption peaks at 3.05 eV (408 nm) and 3.65 eV (340 nm). Moreover, new low-energy transitions are observed at 0.88 eV (1403 nm) and at 1.8–2.0 eV (688–622 nm; Figure S2).

The EPR-silent dianion **Tr**$^{2-}$ is obtained upon further successive contacts with potassium. The optical absorption spectrum of **Tr**$^{2-}$ is quite similar to that of **Tr**$^{\bullet-}$ with a blueshift of the low-energy bands at 1.95 eV (638 nm) and 1.22–1.37 eV (1020–907 nm), whereas peaks within the "vibronic massif" show up at 2.96 eV (420 nm) and 3.60 eV (345 nm). Higher anions could not be isolated, probably due to chemical transformations as the reduction process is continued. These findings may be attributed to possible internal cyclization.[52]

The EPR spectrum of the radical anion **Tr**$^{\bullet-}$ shows a detailed hyperfine pattern (Figure S7), which is understood on considering two sets of three ^{1}H nuclei (4.54, 0.17 MHz) as supported by the ^{1}H ENDOR results (Figure S7b and Table 2).

Additional lines are observed in the wings of the signal. These correspond to the coupling of ^{29}Si and/or ^{13}C nuclei. A satisfying simulation of the experimental spectrum is not at hand as different sets of ^{13}C nuclei lead to equivalent patterns.

Table 3. Relevant structural parameters of the studied OPEs (ADF-BP/TZP). *d* is the interatomic distance; α and β are dihedral angles between successive phenyl rings: $\alpha = (1',2')$; $\beta = (1',3')$.

d [Å]	**M**	**M**$^{\bullet-}$	**T**	**T**$^{\bullet-}$	**T**$^{\bullet3-}$	**P**	**P**$^{\bullet-}$	**P**$^{\bullet3-}$	**Tr**	**Tr**$^{\bullet-}$
C1–C2	1.388	1.387	1.387	1.398	1.400	1.393	1.397	1.399	1.216	1.224
C2–C3	1.389	1.391	1.386	1.382	1.385	1.390	1.385	1.382	1.403	1.391
C3–C4	1.414	1.446	1.420	1.430	1.444	1.418	1.426	1.436	1.417	1.434
C4–C7	1.405	1.394	1.395	1.385	1.383	1.400	1.396	1.388	–	–
C7–C8	1.221	1.231	1.217	1.225	1.232	1.219	1.225	1.230	–	–
C8–C9	–	–	1.401	1.386	1.383	1.400	1.397	1.388	–	–
α [°]	–	–	3.5	3.6	3.1	5.9	0.7	0.3	–	–
β [°]	–	–	–	–	–	2.4	2.4	0.0	–	–

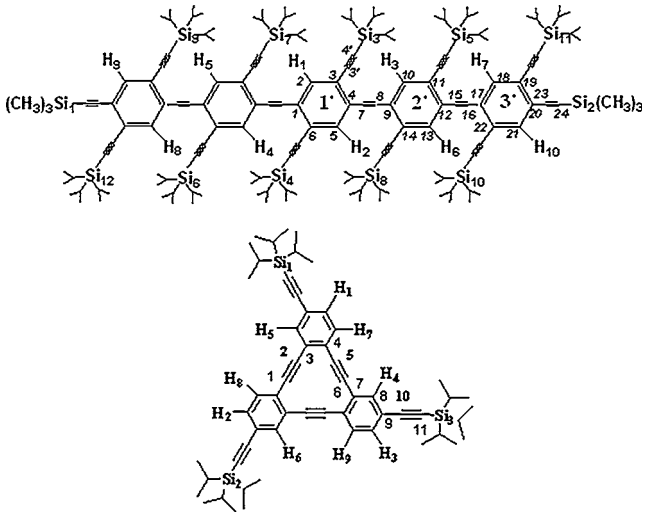

Scheme 2. Atom labeling system for the linear oligomers and **Tr**.

DFT Calculations

Theoretical investigations were performed at the DFT level to rationalize the experimental results. The calculations started from the optimized neutral structures of the entire molecules for all anions. The structures of all of the studied polyanions were further optimized (see Figure S8). Given the large size of the molecules only the conformation of the lowest energy was considered in each case.

Due to the observed slow convergence for **P**$^{\bullet5-}$, the optimization was stopped at a given step to perform a single-point calculation of the EPR properties. Optimized distances and angles computed for neutral and charged species are presented in Table 3, with the atom numbering system given in Scheme 2.

Before listing the main theoretical results for each system, it is worth mentioning from the start that, taken as a whole, the resulting HFCCs calculated at the DFT/B3LYP/6-31 + G(d) level correctly correlate with the corresponding experimental values as long as one considers two subclasses of systems. These classes are easily defined and discussed in the light of Figure 8. The first subclass A contains systems with lower spin density in the singly occupied molecular orbital (SOMO). These are the spatially extended monoanions of the longer oligomers **T**$^{-}$ and **P**$^{-}$. In both cases, the electron spin is delocalized along the central carbon chain (see Figure 9). It can be seen in Figure 8 (trace A, bottom) that the correlation between experimental and DFT-computed HFCCs is linear with an intercept value close to zero. The slope is less than 1, thus pointing to an underestimate of the calculated values with respect to the experimental ones.

The second subclass B comprises systems with higher spin density. These are the shortest monoanions (**M**$^{-}$, **Tr**$^{-}$), and the higher charged states of longer oligomeric trianions (**T**$^{\bullet3-}$, **P**$^{\bullet3-}$) together with the pentaanion **P**$^{\bullet5-}$. As shown by the SOMO spin density, the charges localize at both ends of these molecules. A linear plot yields a slope of 1.09 but with an intercept value of 0.93. Alternatively, a quadratic plot is proposed as a best fit (equation in the legend of Figure 8) with an intercept close to 0. The assignments of subclasses A and B to given nuclei on the molecules will be discussed below for each anion specifically. These are proposed according to both the magnitudes and the numbers of equivalent atoms.

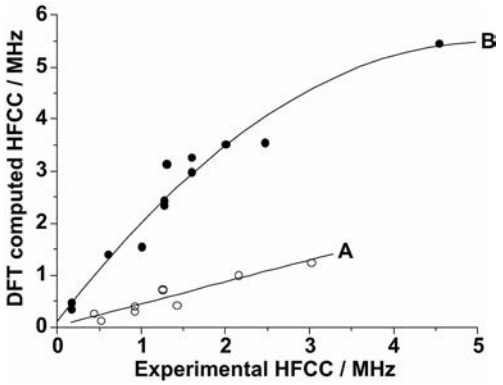

Figure 8. Experimental HFCCs versus DFT-computed HFCCs. A) $\mathbf{T}^{\bullet-}$, $\mathbf{P}^{\bullet-}$; a linear plot yields the following equation: HFCC(DFT) = 0.424 HFCC-(exp) + 0.021 (R^2 = 0.879); B) $\mathbf{M}^{\bullet-}$, $\mathbf{Tr}^{\bullet-}$, $\mathbf{T}^{\bullet3-}$, $\mathbf{P}^{\bullet3-}$, and $\mathbf{P}^{\bullet5-}$; a quadratic plot yields the following equation: HFCC(DFT) = −0.205 HFCC(exp)^2 + 2.097 HFCC-(exp) + 0.116 (R^2 = 0.959).

Subclass A

Geometry optimization of $\mathbf{T}^{\bullet-}$ was performed without any symmetry constraint and the calculated structure does not show significant alteration compared to that of the neutral species **T**, although slight changes in bond lengths are observed (see Table 3). The spatial distribution of the SOMO of the monoanion $\mathbf{T}^{\bullet-}$ is reported in Figure 9. The calculated spin density distribution is extended over the larger conjugated backbone of this oligomer. All DFT-predicted ^{1}H HFCCs for $\mathbf{T}^{\bullet-}$ of the planar conformation are smaller than the experimental ones even with extended basis sets (see Table S1; see also Figure 8 A). Values for the protons H_1 and H_2 are not equivalent (Table 2). The largest HFCCs are mainly due to the protons at positions $H_{3,4,}$ and $H_{5,6}$. The electronic structure of the trimer derivatives with and without side substituents has been shown to be sensitive to the degree of torsion within various conformers.[6,14,19,24] Subsequently, this is investigated in this work (see below).

The hierarchy of the computed ^{1}H HFCCs is of valuable help for the assignment of the experimental values, hence guiding the simulation of the EPR spectra of $\mathbf{P}^{\bullet-}$ (Table 2 and Figure 7). The value of 1.25 MHz for $\mathbf{P}^{\bullet-}$ was attributed to the $H_{7,8,9,10}$ nuclei, whereas the values of 0.92 and 0.52 MHz were assigned to the protons $H_{3,4,5,6}$ and $H_{1,2}$, respectively. The spatial distribution of the SOMO is similar to that of $\mathbf{T}^{\bullet-}$ (Figure 9) with the charge delocalized along the conjugated backbone.

Subclass B

In the case of $\mathbf{M}^{\bullet-}$, high π-spin density is calculated at the central carbon atoms of the phenyl ring (C3, C4, and C6, see

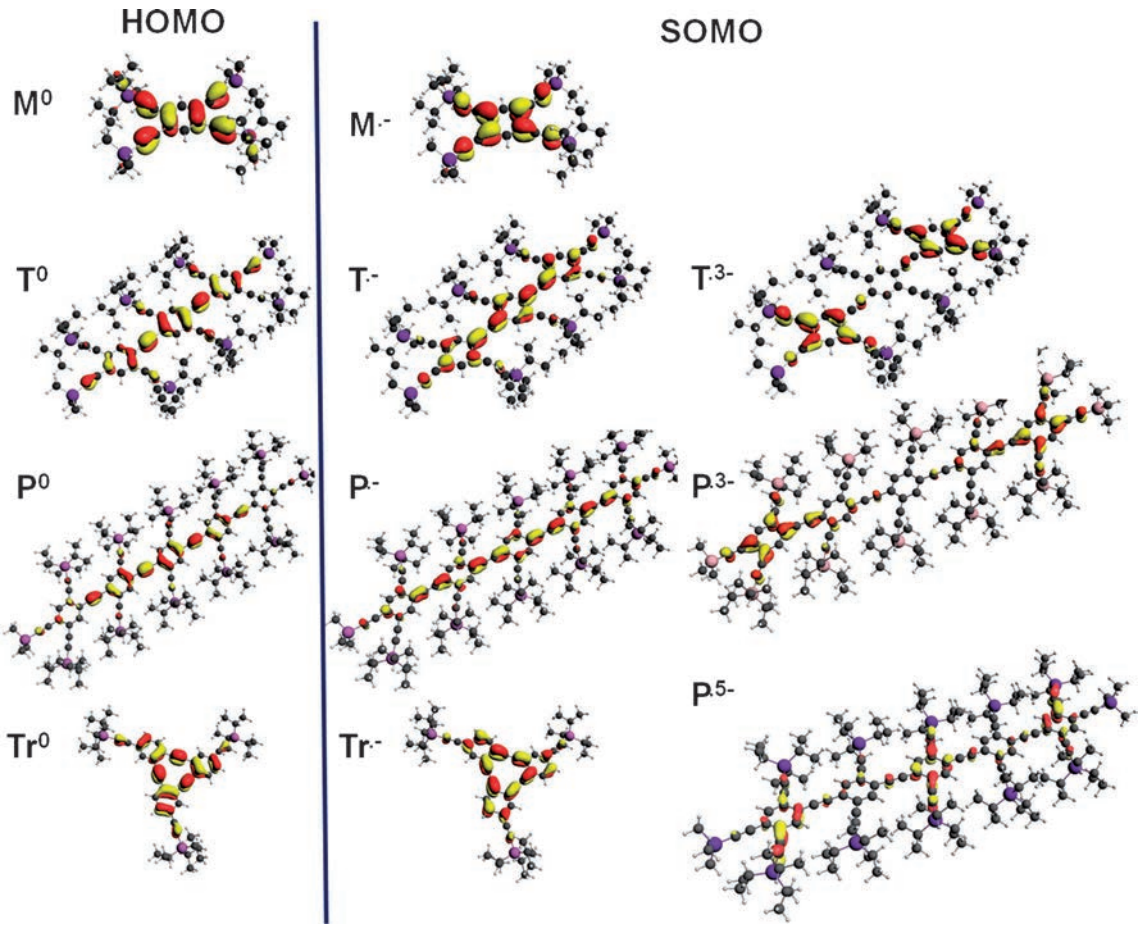

Figure 9. Spatial distribution of the HOMO (left column) for the neutral structure and SOMO (right column) for polyanions.

ring 1′ in Scheme 2) and external carbon atoms (C8 and C4′ bonded to TIPS and TMS, respectively; see Table 4).

The resulting HFCCs calculated at the DFT/B3LYP/6-31 + G(d) level (see Table 2) put $\mathbf{M}^{\bullet-}$ in subclass B (see Figure 8, trace B). The two protons H_1 and H_2 bonded to C2 and C5, respectively, have the same DFT HFCC, that is, 3.55 MHz. They reproduce the central part of the EPR spectrum whereas ^{1}H HFCCs of individual hydrogen atoms on the TMS and TIPS substituents are distributed in a broad range from 0.02 to 3.01 MHz. It is then inferred that the small HFCC in the ENDOR spectrum indicates a rapid rotation of the CH_3 group and leads to the observed average of ^{1}H HFCC.

Further information concerning the spin density distribution may be obtained upon examination of the satellites in the EPR spectrum, which are attributed to the ^{29}Si nuclei. The DFT/B3LYP/6-31 + G(d) calculations show that the four DFT ^{29}Si HFCCs (5.23 and 5.60 MHz) are in the same range but are rather underestimated by a rough factor of 2 on comparison with the experimental values (10.50 MHz). DFT calculations were also carried out with other hybrid functionals and different basis sets (see Table S1).

Increasing the basis set to include diffuse functions results in a better agreement of ^{1}H HFCCs for H_1 and H_2 with the experimental values, although leaving ^{29}Si HFCC underestimated.

No significant geometrical changes are observed on going from $\mathbf{T}^{\bullet-}$ to $\mathbf{T}^{\bullet 3-}$ (see Table 3). DFT calculations were again helpful to assign the measured HFCCs to given ^{1}H nuclei on this molecule. The smallest experimental coupling at 1.0 MHz must be attributed to $H_{5,6}$ (DFT: 1.55 MHz) whereas the remaining two experimental HFCCs at 1.3 and 2.0 MHz correspond to the four nuclei at $H_{1,2,3,4}$ with possible attribution of the largest value to the outer $H_{3,4}$ atoms (DFT: 3.14 and 3.52, respectively). The spatial distribution of the SOMO of $\mathbf{T}^{\bullet 3-}$ is quite different from that of $\mathbf{T}^{\bullet-}$. Although it is quite equally distributed over the conjugated backbone within $\mathbf{T}^{\bullet-}$, it is localized on the external phenyl rings for $\mathbf{T}^{\bullet 3-}$ (Figure 9).

Compared with $\mathbf{T}^{\bullet-}$ the spin density strongly increases on C7, C9, and C11 and the remaining fraction is equally distributed over the carbon backbone until C16 with an extension on the side TIPS arms (Table 4).

In contrast to $\mathbf{P}^{\bullet-}$ and as previously noticed for **T**, DFT calculations of the HFCCs for $\mathbf{P}^{\bullet 3-}$ are greatly overestimated relative to experimental values. The set of protons $H_{3,4,9,10}$, $H_{5,6,7,8}$, and $H_{1,2}$ is ascribed to the HFCC values 1.27, 1.6, and 0.6 MHz, respectively. The calculated structure of $\mathbf{Tr}^{\bullet-}$ does not show significant differences compared to that of the neutral species **Tr**. The SOMO of $\mathbf{Tr}^{\bullet-}$ is spread out over the central ring and on external carbon atoms on the phenyl ring and TIPS (see Figure 9). The calculated HFCCs are in accordance with experimental values. The highest coupling at 4.54 MHz can be assigned to the protons $H_{1,2,3}$ whereas the value of 0.17 MHz was attributed to the $H_{4,5,6}$ or $H_{7,8,9}$ nuclei. For $\mathbf{P}^{\bullet 5-}$, the spatial distribution is mainly delocalized on the central ring and the two external rings. If we refer to Figure 8, the place of $\mathbf{P}^{\bullet 5-}$ is in subclass B.

Table 4. Selected computed Mulliken atomic spin densities at the B3LYP/6-31 + G(d) level.

	$\mathbf{M}^{\bullet-}$	$\mathbf{T}^{\bullet-}$	$\mathbf{T}^{\bullet 3-}$	$\mathbf{P}^{\bullet-}$	$\mathbf{P}^{\bullet 3-}$	$\mathbf{P}^{\bullet 5-}$	$\mathbf{Tr}^{\bullet-}$
C1	0.194	0.082	−0.08	0.044	−0.064	0.077	0.008
C2	−0.08	−0.014	0.046	0.041	−0.069	0.082	0.061
C3	0.179	0.070	−0.063	−0.006	0.032	−0.040	0.042
C3′							
C4	0.186	0.080	−0.080	0.050	−0.082	0.090	0.108
C4′							
C5	−0.076	−0.012	0.048	0.037	−0.054	0.069	0.007
C6	0.172	0.068	−0.06	−0.002	0.018	−0.037	0.062
C7	−0.058	0.012	0.103	0.020	0.048	−0.072	0.042
C8	0.142	0.054	−0.108	0.028	−0.078	0.082	−0.02
C9	–	0.030	0.138	0.036	0.056	−0.068	0.042
C10	–	0.010	−0.062	0.047	−0.052	−0.009	0.083
C11	–	0.018	0.142	−0.009	0.045	0.014	−0.014
C12	–	0.098	0.084	0.052	−0.060	−0.017	−0.015
C13	–	−0.032	−0.033	0.032	0.052	−0.063	0.038
C14	–	0.085	0.090	0.001	−0.040	0.039	–
C15	–	−0.030	−0.021	0.000	0.110	0.038	–
C16	–	0.067	0.074	0.040	−0.070	−0.045	–
C17	–	–	-	0.011	0.123	0.062	–
C18	–	–	-	0.043	0.137	0.042	–
C19	–	–	-	−0.017	−0.050	−0.027	–
C20	–	–	–	0.051	0.144	0.047	–
C21	–	–	–	0.005	0.116	0.049	–
C22	–	–	–	0.008	−0.058	0.00	–
C23	–	–	–	−0.019	−0.046	−0.011	–
C24	–	–	–	0.040	0.117	0.039	–
Si1	0.017	0.003	0.028	0.002	0.021	0.125	0.004
Si2	0.020	0.003	0.028	0.002	0.033	0.19	0.004
Si3	0.049	0.007	−0.021	0.002	−0.008	−0.042	0.006
Si4	0.031	0.007	−0.021	0.004	−0.012	−0.040	–
Si5	–	0.002	0.08	0.000	0.000	−0.008	–
Si7	–	–	0.058	0.004	0.000	−0.008	–
Si9	–	–	–	0.004	0.033	−0.008	–
Si11	–	–	–	0.000	0.030	−1.10	–

3. Discussion

As previously noticed, geometrical parameters and HFCCs determined from DFT calculations allow the identification of the EPR signatures for all reduced species. For the studied series, nearly identical bond lengths are found for neutral molecules, monoanions, and trianions. Table 3 reports only significant variations of bond length and/or molecular conformation along the PE main chain.

Successive additions of electrons on **T** leave unchanged the dihedral angle between phenyl rings 1′ and 2′, whereas **P** be-

comes planar upon being charged (5.9° to 0°). Therefore, a better π conjugation is expected as the size of the oligomer is extended. Notably, such molecules have a nearly planar ladder skeleton in spite of the presence of bulky TIPS substituents. Moreover, the molecular conformation is not at all or only slightly affected as the number of added electrons increases. The shortest bond lengths are found for the ethynyl connection, as expected for a triple bond. The computed changes in distances for the monoanions can be rationalized upon examination of the properties of the frontier MOs.

The LUMOs show a bonding character between C7 and C8, whereas the phenyl rings are essentially aromatic. Adding one electron leads to an antibonding character with lengthening of the C7–C8 bond (1.225 vs 1.217 Å for **T**; 1.225 vs 1.219 Å for **P**) and the phenyl ring becomes quinoid-like. It is expected beyond a better π conjugation between the phenyl units. The shapes of the frontier orbitals are quite similar for the neutral **M**, **T**, and **P**. For a given oligomer, successive reductions may be roughly considered as adding electrons to the LUMO and LUMO + 1 orbitals of the neutral species. This is exemplified in Figure S9, in which the SOMO of the trianionic radical species $\mathbf{T}^{3-}$ resembles the corresponding LUMO of the dianionic diamagnetic species $\mathbf{T}^{2-}$. Accordingly, the SOMO of $\mathbf{T}^{\bullet-}$ looks like the LUMO of the neutral **T**. Examination of the frontier MOs of higher charged species $\mathbf{M}^{\bullet 3-}$ and $\mathbf{P}^{\bullet 3-}$ shows that these SOMOs are predominantly localized in the external part of the molecules whereas the SOMO−1 MOs have a shape similar to that of the SOMOs of the corresponding radical anions. We have previously mentioned the possible mixture of two conformers to account for the indetermination in the EPR/ENDOR spectra of $\mathbf{T}^{\bullet-}$. This assumes their coexistence at or close to room temperature. The effects of molecular conformation on the electronic properties have been much investigated, mostly through DFT for **T** and **P** OPEs with various side and terminal substituents with respect to photophysical properties[23,24] or single-molecule conductance.[12–14] As a summary, the conjugation/electronic delocalization over the OPE is broken with the molecular twist around the principal axis of these linear OPEs. To check this point, the conformational energies of neutral **T** and charged $\mathbf{T}^{\bullet-}$ were computed at the ADF DFT level for various dihedral angles θ corresponding to rotation about the C8–C9 bond (see Scheme 2 for the numbering system), whereas the central phenyl ring and its neighboring triple bond were kept coplanar (see Figure S10).

As the dihedral angle increases by about 30° a maximum energy is obtained due to the loss of the π-electron delocalization. More stable conformations are computed for a dihedral angle close to 0° and 60°, the energy barrier being approximately 10 kcal mol^{-1}. The corresponding $E(\theta)$ curve of $\mathbf{T}^{\bullet-1}$ shows a similar variation to that of the neutral species. In contrast to the present results, the rotation barrier of OPEs is usually considered to be low, of the order of 1 kcal mol^{-1} or less.[14,20,53] The high rotation barrier found for TIPS-protected OPEs probably results from steric hindrance between neighboring bulky TIPS substituents. It is shown that two distinct rotational conformers may coexist on both sides of the rotational barrier. It is suggested that this is the explanation for the apparent mismatch between ENDOR and EPR for the radical anion $\mathbf{T}^{\bullet-}$. The thermal equilibrium builds up a conformational average of all of the accessible rotational conformers. The statistical average is expected to be energetically closer to the real system than that computed for the trimer of lowest energy. This is why the resulting EPR spectrum of the $\mathbf{P}^{\bullet-}$ radical anion does not show a detailed structure. These have been most probably smeared out through conformational averaging. The literature also mentioned the possibility of ion-pair formation in THF solvent,[54] but in our case we did not observe splitting by potassium in dilute solution.

A comparison between the calculated HFCC values for monoanions suggests that the spin density is delocalized along the carbon backbone as the molecule grows. As a matter of fact, calculated HFCCs for the monoanions at position $H_{1,2}$ decrease from $\mathbf{M}^{\bullet-}$ to $\mathbf{P}^{\bullet-}$, the same trend being observed for $H_{3,4}$ and $H_{5,6}$. This is consistent with the experimental ^{1}H HFCCs measured in ENDOR spectra. It points to a fully delocalized spin species for the monoanions, as already observed for oligoperinaphthalenes.[40,46]

Dianion derivatives may exist as triplet or singlet ground states. The singlet state has been computed as an open-shell derivative and it is found to be lower in energy than the triplet state for the three species **M**, **T**, and **P**. This is in line with EPR spectroscopy in which the evenly charged species are silent suggesting the $S = 0$ ground state. It is suggested that the spin state S_n for n electrons is given by simple arithmetic: $S_n = 0$ for even n, and $S_n = {}^1/_2$ for odd n. Therefore, the odd number of electrons results in a radical anion with a doublet spin multiplicity, whereas even-numbered anions are in a singlet $S = 0$ state, which is EPR silent. To support this scheme for the evolution of the electronic structure of the successive anions of **T**, the intensity of the EPR signal (double integral of the first derivative of the absorption line) was assessed for two solutions of $\mathbf{T}^{\bullet-}$ and $\mathbf{T}^{3-}$ of known concentration deduced from UV/Vis spectroscopy. This is proportional to the spin susceptibility, and hence to the spin concentration for paramagnetic species according to the Curie law. The absolute spin concentration within the solutions could not be calibrated accurately. However, the relative value between the two solutions is quite accurate. It is found that the number of spins per molecule is the same in both samples. It means that the trianion should be viewed as a single $S = {}^1/_2$ spin. Moreover, to ascertain this proposal the temperature dependence of the EPR susceptibility was recorded in the 4–100 K temperature range. It shows a pure Curie law (Figure S11) as expected for an isolated $S = {}^1/_2$ spin.

The ^{1}H ENDOR spectra of trianions indicate spin density redistribution. Given the observed smaller number of ^{1}H HFCCs, the simulation of the EPR spectra of $\mathbf{T}^{\bullet 3-}$ and $\mathbf{P}^{\bullet 3-}$ is more straightforward than for the corresponding monoanions. DFT calculations show that, in contrast to the monoanions, the calculated spin density is mainly located on the outer PE unit for the trianions. For instance, the spin density on C24 is three times greater for $\mathbf{P}^{\bullet 3-}$ than $\mathbf{P}^{\bullet-}$. Consequently, the addition of a third electron probably drives the system to a more coplanar conformation. This trend is also corroborated by the NIR ab-

sorption band, which is blueshifted at increasing charge, thus suggesting that for a given oligomer electrons are more localized as the charge increases. Note also that pentaanion $\mathbf{P}^{\bullet 5-}$ is characterized by an EPR spectrum similar in shape to that of $\mathbf{M}^{\bullet -}$ with a triplet 1-2-1 and a close ^{1}H HFCC (2.47 vs 3.08 MHz for $\mathbf{M}^{\bullet -}$ and $\mathbf{P}^{\bullet 5-}$). The spatial distribution of the SOMO is in accordance with the assignment of subclass B.

Spectroscopic properties (optical and EPR) of the unsubstituted **Tr** were described earlier.[55,56] The addition of the TIPS substituent was considered as an inductive effect. Indeed, a redshift is observed on UV/Vis spectra. Unfortunately, the impossibility of obtaining a higher anion than the divalent one discards the appealing possibility of comparing the electron/spin density distribution over the linear $\mathbf{T}^{\bullet 3-}$ and triangular $\mathbf{Tr}^{\bullet 3-}$ trianion with respect to the corresponding monoanions. Considering the neutral **Tr** and the anionic $\mathbf{Tr}^{\bullet -}$ structures, DFT computations show appreciable changes in individual bond lengths. Upon one-electron reduction the C1–C2 and C3–C4 distances increase greatly (1.216 vs 1.224 Å and 1.417 vs 1.434 Å). This probably results from intramolecular oligocyclization upon further electron addition, thus corroborating experimental failures to obtain higher stable anions.[52,57]

Frontier orbitals of neutral and monoanionic species of **Tr** and **T** are similar (Figure 9). The electron density in each HOMO is delocalized on the phenyl ring and on the ethynyl bond, whereas the LUMO is regularly distributed along the backbone for **T** and over the ring for **Tr**. This inner-ring electronic distribution for **Tr** is appealing for metal inclusion compounds.

The UV/Vis-NIR spectra of the series of neutral oligomers have been previously discussed.[47] The present discussion will thus consider the previous experimental data and conclusions in the light of DFT calculations (HOMO–LUMO energy gap: HLG). As expected, a bathochromic shift has been reported previously for neutral compounds as the size of the oligomer increases. This indicates the increasing electronic delocalization length usually related to π conjugation. The pentamer appears as the precursor to an infinitely conjugated chain, that is, the polymer. It was suggested[47] that the electron-donating nature of TIPS groups may lower the HLG relative to unsubstituted or other side alkyl-substituted OPEs. As a matter of fact the UV/Vis main absorption band of OPEs is usually found between approximately 3.1 and 4.1 eV.[8] The **T**, **P**, and **M** compounds show the UV/Vis main absorption peak below 3.1 eV. Table 5 summarizes the optical absorption spectroscopic data for neutral **T**, **P**, and **M** and their successive anions.

The plot of the energy of the experimental main absorption peaks of neutral, monoanionic, dianionic, and trianionic **M**, **T**, and **P** versus $1/n$, in which n is the number of PE units ($n = 1$, 3, 5 for **M**, **T**, **P**, respectively), shows the expected linear decrease, that is, a redshift for all transitions upon increasing the conjugation length (see Figure S12A). Notably, this redshift is more pronounced for the dianions and trianions than for the neutral species and the monoanions. The extrapolation of the line to the infinite chain ($1/n = 0$) yields an estimation of the HLG at the limiting effective conjugation length.[58–60] These features, although underestimated relative to the experimental data, are still quite well reproduced by DFT computations, which yield a linear correlation for the plot of the HLG of the neutral species versus $1/n$ (see Figures S12B and S13).

Table 5. UV/Vis–NIR peak positions [eV] of neutral species (N), monoanion radical (RA), dianions (DA), trianions (TRA), tetraanions (TTA), and pentaanions (PA). High- and low-energy absorptions are labeled 1 and 2, respectively, and the higher-intensity absorption is given in bold characters.

	M	T	P	Tr
N1	**4.51**	**4.48**	**4.31**	**3.90**
N2	4.01	3.52	3.28	
RA1	2.89;2.73		4.40	**3.65**;3.04
RA2	**2.07**;1.85	**2.03**;1.38	**1.95**	1.99;1.80
RA3		0.84;0.81;**0.65**	0.55	0.88
DA1	4.56;3.62;2.88	4.34;3.31	4.38	3.60;**2.95**
DA2	**2.41**;1.84	1.35;1.00;**0.83**	2.25;**0.63**	**1.94**;1.37;1.21
TRA1	–	3.31	4.36	
TRA2	–	**1.48**;0.98	**0.76**	
TTA1	–	–	3.60	
TTA2	–	–	**1.33**	
PA1	–	–	2.92	

Compared with neutral compounds, the spectra of all of the charged species up to the trianions have been shown to exhibit additional low-energy peaks in the NIR region below approximately 2 eV. Radical monoanions $\mathbf{T}^{\bullet -}$, $\mathbf{P}^{\bullet -}$, and $\mathbf{Tr}^{\bullet -}$ are characterized by two additional and distinct low-energy peaks, whereas polyanions show only one such low-energy peak. For a given oligomer these NIR peaks are blueshifted as the charge increases, thus indicating increasing electronic localization. This effect is nicely supported by EPR HFCCs and corroborated by the DFT computations with the increase of the HFCC values on the central phenyl ring as the anion order increases (Figure 9 and Table 4).

For the radical anions the energy (1.95 eV) deduced from the extrapolation of the line RA2 in Figure S12A is much lower than the corresponding value for the neutral derivative (3.16 eV). Moreover, it is close to the value deduced from cyclic voltammetry (1.72 eV). Indeed, a similar plot to Figure S12C with the reduction potential E_{red} versus $1/n$ yields linear variations for the first and the second reduction steps. Such evolution is frequently observed for conjugated oligomers.[58,61]

4. Conclusions

Detailed studies of the electronic structure of up to five consecutive redox states of substituted TIPS-OPEs of increasing length, from the monomer **M**, trimer **T**, up to the pentamer **P**, were achieved. A cyclic triangular annulene, **Tr**, was also investigated to compare its properties with those of the corresponding linear trimer. The doping of these series of oligomers was performed on a K mirror. The monitoring of the successive doping sequences by UV/Vis spectroscopy showed clear isosbestic points on going from the neutral species to the various charged states. It is shown that the oligomer of order n ($n = 1$, 3, 5) may accommodate in a stable state up to n electrons and even more in the case of the trimer. The ability of these OPEs to behave as electron reservoirs is thus demonstrated. Each of

the successive anionic species was generated in a stable state at room temperature if kept under sealed EPR tubes. EPR/ENDOR spectra were consequently recorded to investigate their electronic properties. It is shown that addition of an odd number of electrons results in a paramagnetic spin doublet state. On the other hand, the addition of an even number of electrons does not show any EPR response. This EPR-silent state is consequently attributed to the strong spin pairing of electrons resulting in a singlet ground state. DFT calculations (B3LYP/6-31 + (d,p)) helped to assign the HFCCs to the corresponding nuclei for the radical monoanions and trianions. The resulting HFCCs correlate correctly with the corresponding experimental values as long as one considers two subclasses of systems. It is shown that whereas the radical monoanion is well delocalized over the carbon spine of the oligomers, radical trianions and pentaanions tend to localize at the phenyl ring termini. This is qualitatively corroborated by UV/Vis spectroscopy, which showed that there is a blueshift of the low-energy transitions appearing during doping upon going from the monoanion to the higher charged states. As expected, the conjugation length is extended as the oligomer size is increased. This is indicated by a redshift of the overall optical absorption bands of the oligomers on going from **M** to **P**.

Experimental Section

Compounds

The procedure to synthesize the OPEs ($n = 1$, 3 ,5; respectively **M**, **T** ,**P**) and 4,4′,4″-tris(triisopropylsilylethynyl)dehydro-tribenzo[12]annulene (**Tr**) has been described previously.[47]

Spectroscopy

Tetrahydrofuran (THF) was used as the solvent for all studies. To avoid protonation of the charged species, THF free of protonic impurities was distilled through a vacuum line directly into the apparatus from a purple solution of the sodium salt of the benzophenone dianion. The UV/Vis-NIR spectra were recorded with a Varian Cary500 spectrophotometer. EPR/ENDOR spectra were recorded on a Bruker spectrometer ESP 300 equipped with a radio-frequency amplifier EMI 500. The multiply charged anions were generated by bringing a solution of the substrate (10^{-4} M) in THF into contact with a potassium mirror in a specially designed glass apparatus sealed under high vacuum. A quartz optical cell and quartz tubes attached to the apparatus allowed in situ optical and EPR measurements. Increasing the reduction states of the compounds was achieved by successive contact of the solution with the potassium. Progression of the reduction process was monitored by recording optical absorption and EPR spectra.

Electrochemistry

Cyclic voltammetry at scan rates ranging from 0.1 to 100 $V s^{-1}$ was carried out in a homemade cell connected to a vacuum line. The cell was a classical three-electrode cell: the working electrode was a platinum disk (1 mm diameter) sealed in glass and polished with 0.5 to 2 μm diamond paste. The counter electrode was a platinum wire and the pseudo reference electrode a silver wire. The right amount of supporting electrolyte, ferrocene, used as internal standard, and the species were put in the cell and placed under vacuum for 24 h. Afterwards, the THF was transferred to the cell using deep-freeze techniques. The cell was connected to a computerized multipurpose electrochemical device Autolab PGSTAT 30 (Eco Chemie B.V., The Netherlands), driven by GPES software running on a personal computer.

DFT Calculations

Ground-state electronic structures were calculated by DFT methods using the Amsterdam density functional (ADF2003.01)[62] and Gaussian 03[63] software packages. Calculations for all species were performed without any constrained symmetry. Electron correlation was treated within the local density approximation in the Vosko–Wilk–Nusair parameterization.[64] Electronic configurations of atoms were described by a triple-Slater-type orbital basis set. EPR properties were calculated on a single point of the optimized structure 6-31 + G(d) for the Gaussian 03 package. Representations of the molecular structures and orbitals were made using ADF-view v06.

Acknowledgements

This work was supported by the Centre National de la Recherche Scientifique and the Université of Strasbourg (Strasbourg, France; UMR 7177 and UPR 22, CNRS). We thank the Ministère de l'Enseignement Supérieur et de la Recherche for a PhD fellowship (A.A.) and Daniel Schwartz (IUT Robert Schuman, Strasbourg) for proofreading of this article.

Keywords: density functional calculations · electronic structure · ENDOR spectroscopy · EPR spectroscopy · polyanions

[1] A. J. Heeger, H. MacDiarmid, H. Shirakawa in The Nobel Prize in Chemistry 2000, http://www.nobelprize.org/nobel_prizes/chemistry/laureates/2000/.
[2] V. Coropceanu, J. Cornil, D. A. da Silva, Y. Olivier, R. Silbey, J. L. Bredas, *Chem. Rev.* **2007**, *107*, 926 – 952.
[3] T. A. Skotheim, J. R. Reynolds, *Handbook of Conducting Polymers*, CRC, Boca Raton, FL, **2007**.
[4] C. Li, M. Liu, N. G. Pschirer, M. Baumgarten, K. Muellen, *Chem. Rev.* **2010**, *110*, 6817 – 6855.
[5] R. Kiebooms, R. Menon, K. Lee, *Conducting Polymers*, Academic Press, New York, **2001**.
[6] M. Aschi, M. D'Alessandro, M. Pellegrino, A. Di Nola, M. D'Abramo, A. Amadei, *Theor. Chem. Acc.* **2008**, *119*, 469 – 476.
[7] L. A. Bumm, J. J. Arnold, M. T. Cygan, T. D. Dunbar, T. P. Burgin, L. Jones, D. L. Allara, J. M. Tour, P. S. Weiss, *Science* **1996**, *271*, 1705 – 1707.
[8] U. H. F. Bunz, *Chem. Rev.* **2000**, *100*, 1605 – 1644.
[9] F. R. F. Fan, R. Y. Lai, J. Cornil, Y. Karzazi, J. L. Bredas, L. T. Cai, L. Cheng, Y. X. Yao, D. W. Price, S. M. Dirk, J. M. Tour, A. J. Bard, *J. Am. Chem. Soc.* **2004**, *126*, 2568 – 2573.
[10] K. Liu, G. R. Li, X. H. Wang, F. S. Wang, *J. Phys. Chem. C* **2008**, *112*, 4342 – 4349.
[11] Q. Lu, K. Liu, H. M. Zhang, Z. B. Du, X. H. Wang, F. S. Wang, *ACS Nano* **2009**, *3*, 3861 – 3868.
[12] S. W. Robey, J. W. Ciszek, J. M. Tour, *J. Phys. Chem. C* **2007**, *111*, 17206 – 17212.
[13] J. M. Seminario, A. G. Zacarias, P. A. Derosa, *J. Chem. Phys.* **2002**, *116*, 1671 – 1683.
[14] J. M. Seminario, A. G. Zacarias, J. M. Tour, *J. Am. Chem. Soc.* **2000**, *122*, 3015 – 3020.
[15] J. M. Tour, *Acc. Chem. Res.* **2000**, *33*, 791 – 804.
[16] A. Villares, D. P. Lydon, P. J. Low, B. J. Robinson, G. J. Ashwell, F. M. Royo, P. Cea, *Chem. Mater.* **2008**, *20*, 258 – 264.

[17] H. P. Yoon, M. M. Maitani, O. M. Cabarcos, L. T. Cai, T. S. Mayer, D. L. Allara, *Nano Lett.* **2010**, *10*, 2897 – 2902.
[18] A. Beeby, K. Findlay, P. J. Low, T. B. Marder, *J. Am. Chem. Soc.* **2002**, *124*, 8280 – 8284.
[19] P. V. James, P. K. Sudeep, C. H. Suresh, K. G. Thomas, *J. Phys. Chem. A* **2006**, *110*, 4329 – 4337.
[20] N. Li, K. Jia, S. Wang, A. Xia, *J. Phys. Chem. A* **2007**, *111*, 9393 – 9398.
[21] S. Anderson, *Chem. Eur. J.* **2001**, *7*, 4706 – 4714.
[22] W. Hu, Q. F. Yan, D. H. Zhao, *Chem. Eur. J.* **2011**, *17*, 7087 – 7094.
[23] A. D. Slepkov, F. A. Hegmann, S. Eisler, E. Elliott, R. R. Tykwinski, *J. Chem. Phys.* **2004**, *120*, 6807 – 6810.
[24] Y. L. Tang, E. H. Hill, Z. J. Zhou, D. G. Evans, K. S. Schanze, D. G. Whitten, *Langmuir* **2011**, *27*, 4945 – 4955.
[25] Y. L. Tang, Z. J. Zhou, K. Ogawa, G. P. Lopez, K. S. Schanze, D. G. Whitten, *Langmuir* **2009**, *25*, 21 – 25.
[26] C. S. Wang, A. S. Batsanov, M. R. Bryce, *Faraday Discuss.* **2006**, *131*, 221 – 234.
[27] P. Wautelet, M. Moroni, L. Oswald, J. LeMoigne, A. Pham, J. Y. Bigot, S. Luzzati, *Macromolecules* **1996**, *29*, 446 – 455.
[28] Y. Yamaguchi, Y. Shimoi, T. Ochi, T. Wakamiya, Y. Matsubara, Z. I. Yoshida, *J. Phys. Chem. A* **2008**, *112*, 5074 – 5084.
[29] S. C. Yuan, S. L. Han, X. Ge, H. C. Wang, *Chin. Chem. Lett.* **2010**, *21*, 97 – 100.
[30] Y. G. Zhi, S. W. Lai, Q. K. W. Chan, Y. C. Law, G. S. M. Tong, C. M. Che, *Eur. J. Org. Chem.* **2006**, 3125 – 3139.
[31] C. Z. Zhou, T. X. Liu, J. M. Xu, Z. K. Chen, *Macromolecules* **2003**, *36*, 1457 – 1464.
[32] R. B. Breitenkamp, G. N. Tew, *Macromolecules* **2004**, *37*, 1163 – 1165.
[33] Q. H. Chu, Y. Pang, *Macromolecules* **2003**, *36*, 4614 – 4618.
[34] J. L. Brédas, R. R. Chance, R. Silbey, *Phys. Rev. B* **1982**, *26*, 5843 – 5854.
[35] J. L. Bredas, G. B. Street, *Acc. Chem. Res.* **1985**, *18*, 309 – 315.
[36] Y. Furukawa, *J. Phys. Chem.* **1996**, *100*, 15644 – 15653.
[37] A. O. Patil, A. J. Heeger, F. Wudl, *Chem. Rev.* **1988**, *88*, 183 – 200.
[38] A. Alberti, B. Ballarin, M. Guerra, D. Macciantelli, A. Mucci, F. Parenti, L. Schenetti, R. Seeber, C. Zanardi, *ChemPhysChem* **2003**, *4*, 1216 – 1225.
[39] J. J. Apperloo, J. M. Raimundo, P. Frere, J. Roncali, R. A. J. Janssen, *Chem. Eur. J.* **2000**, *6*, 1698 – 1707.
[40] M. Baumgarten, K. H. Koch, K. Mullen, *J. Am. Chem. Soc.* **1994**, *116*, 7341 – 7348.
[41] S. Choua, A. Jouaiti, M. Geoffroy, *Phys. Chem. Chem. Phys.* **1999**, *1*, 3557 – 3560.
[42] F. Gerson, W. Huber, *Acc. Chem. Res.* **1987**, *20*, 85 – 90.
[43] U. Mueller, M. Baumgarten, *J. Am. Chem. Soc.* **1995**, *117*, 5840 – 5850.
[44] A. Österholm, A. Petr, C. Kvarnstrom, A. Ivaska, L. Dunsch, *J. Phys. Chem. B* **2008**, *112*, 14149 – 14157.
[45] D. Rohde, L. Dunsch, A. Tabet, H. Hartmann, J. Fabian, *J. Phys. Chem. B* **2006**, *110*, 8223 – 8231.
[46] C. Onitsch, A. Rosspeintner, G. Angulo, M. Griesser, M. Kivala, B. Frank, F. Diederich, G. Gescheidt, *J. Org. Chem.* **2011**, *76*, 5628 – 5635.
[47] A. Al Ouahabi, P. N. W. Baxter, J. P. Gisselbrecht, A. De Cian, L. Brelot, N. Kyritsakas-Gruber, *J. Org. Chem.* **2009**, *74*, 4675 – 4689.
[48] P. Turek, P. Wautelet, J. LeMoigne, J. L. Stanger, J. J. Andre, A. Bieber, P. Rey, A. DeCian, J. Fischer, *Mol. Cryst. Liq. Crys. A* **1995**, *271*, A99 – A108.
[49] P. Wautelet, L. Catala, A. Bieber, P. Turek, J. J. Andre, *Polyhedron* **2001**, *20*, 1571 – 1576.
[50] P. Wautelet, J. Le Moigne, V. Videva, P. Turek, *J. Org. Chem.* **2003**, *68*, 8025 – 8036.
[51] J. Bartoszewicz, G. L. Hug, M. Pietrzak, H. Kozubek, J. Paczkowski, B. Marciniak, *Macromolecules* **2007**, *40*, 8642 – 8648.
[52] D. Malaba, A. Djebli, L. Chen, E. A. Zarate, C. A. Tessier, W. J. Youngs, *Organometallics* **1993**, *12*, 1266 – 1276.
[53] S. Karabunarliev, M. Baumgarten, K. Mullen, *J. Phys. Chem. A* **2000**, *104*, 8236 – 8243.
[54] L. Lee, R. Adams, J. Jagur-Grodzinski, M. Szwarc, *J. Am. Chem. Soc.* **1971**, *93*, 4149 – 4154.
[55] H. Brunner, K. H. Hausser, M. Rawitscher, H. A. Staab, *Tetrahedron Lett.* **1966**, *7*, 2775 – 2779.
[56] R. E. Koning, P. J. Zandstra, *Chem. Phys. Lett.* **1978**, *56*, 322 – 325.
[57] W. J. D. Youngs, C. A. Tessier, *Organometallics* **1991**, *10*, 2089 – 2090.
[58] J. L. Bredas, R. Silbey, D. S. Boudreaux, R. R. Chance, *J. Am. Chem. Soc.* **1983**, *105*, 6555 – 6559.
[59] H. Kuhn, *J. Chem. Phys.* **1949**, *17*, 1198 – 1212.
[60] L. M. Tolbert, *Acc. Chem. Res.* **1992**, *25*, 561 – 568.
[61] J. Anthony, C. Boudon, F. Diederich, J. P. Gisselbrecht, V. Gramlich, M. Gross, M. Hobi, P. Seiler, *Angew. Chem.* **1994**, *106*, 794 – 798; *Angew. Chem. Int. Ed. Engl.* **1994**, *33*, 763 – 766.
[62] ADF2002.03, SCM, Theoretical Chemistry, Vrije Universiteit, Amsterdam, The Netherlands, http://www.scm.com; G. te Velde, F. M. Bickelhaupt, S. J. A. van Gisbergen, C. Fonseca Guerra, E. J. Baerends, J. G. Snijders, T. Ziegler, "Chemistry with ADF", *J. Comput. Chem.* **2001**, *22*, 931 – 967; C. Fonseca Guerra, J. G. Snijders, G. te Velde, E. J. Baerends, *Theor. Chem. Acc.* **1998**, *99*, 391.
[63] *Gaussian 03 (Revision C.02)*, M. J. Frisch, G. W. Trucks, H. B. Schlegel, G. E. Scuseria, M. A. Robb, J. R. Cheeseman, J. A. Montgomery, T. Vreven, K. N. Kudin, J. C. Burant, J. M. Millam, S. S. Iyengar, J. Tomasi, V. Barone, B. Mennucci, M. Cossi, G. Scalmani, N. Rega, G. A. Petersson, H. Nakatsuji, M. Hada, M. Ehara, K. Toyota, R. Fukuda, J. Hasegawa, M. Ishida, T. Nakajima, Y. Honda, O. Kitao, H. Nakai, M. Klene, X. Li, J. E. Knox, H. P. Hratchian, J. B. Cross, C. Adamo, J. Jaramillo, R. Gomperts, R. E. Stratmann, O. Yazyev, A. J. Austin, R. Cammi, C. Pomelli, J. W. Ochterski, P. Y. Ayala, K. Morokuma, G. A. Voth, P. Salvador, J. J. Dannenberg, V. G. Zakrzewski, S. Dapprich, A. D. Daniels, M. C. Strain, O. Farkas, D. K. Malick, A. D. Rabuck, K. Raghavachari, J. B. Foresman, J. V. Ortiz, Q. Cui, A. G. Baboul, S. Clifford, J. Cioslowski, B. B. Stefanov, G. Liu, A. Liashenko, P. Piskorz, I. Komaromi, R. L. Martin, D. J. Fox, T. Keith, M. A. Al-Laham, C. Y. Peng, A. Nanayakkara, M. Challacombe, P. M. W. Gill, B. Johnson, W. Chen, M. W. Wong, C. Gonzalez, J. A. Pople, Gaussian, Inc., Wallingford CT, **2004**.
[64] S. H. Vosko, L. Wilk, M. Nusair, *Can. J. Phys.* **1980**, *58*, 1200 – 1211.